Journal of Materials Chemistry C

ROYAL SOCIETY OF CHEMISTRY

PAPER

View Article Online
View Journal | View Issue

Cite this: J. Mater. Chem. C, 2021, 9, 4978

A tailorable polarity-flipping response in self-powered, flexible Sb_2Se_3/ZnO bilayer photodetectors†

Jinchun Jiang, ‡[a] Yujie Guo, ‡[a] Xiaoliang Weng,[a] Fangchao Long,[a] Yun Xin, [ab] Yangfan Lu,[b] Zhizhen Ye,[b] Shuangchen Ruan [a] and Yu-Jia Zeng *[a]

The new era of the Internet of Things has spawned research into multifunctional photodetectors. Herein, the intriguing features of dual-polarity and flexibility are creatively embraced in Sb_2Se_3/ZnO bilayer photodetectors. The current reversal, with respect to the incident wavelengths, originates from the synergy of photovoltaic and photo-thermoelectric effects. An unprecedented polarity-double-flipping phenomenon was discovered at a critical thickness of the ZnO capping layer. The dual-polarity response is tailorable, as it is critically dependent on the band alignment, light penetration depth, and interfacial properties of the heterostructure. The optimal device has superior overall performance in terms of the response bandwidth, responsivity, detectivity, and response speed. The flexible devices can withstand 600 bending cycles with only a 4.38% degradation in the performance and a well-localized polarity-flipping wavelength. This study shows that the Sb_2Se_3/ZnO photodetector has excellent potential for use in bipolar signal communications in wireless, filterless, and wearable optoelectronic systems. It also paves the way for the design and optimization of flexible dual-polarity photodetectors from arbitrary hetero-assemblies.

Received 18th February 2021,
Accepted 17th March 2021

DOI: 10.1039/d1tc00786f

rsc.li/materials-c

Introduction

Wearable photodetectors (PDs) are enticing building blocks for imaging, sensing, optical communications and environmental monitoring in the new era of the Internet of Things.[1–4] The device reliability relies primarily on its durability against repetitive folding, bending and stretching.[5] In the current market, most flexible substrates used to integrate PDs only resist processing temperatures up to 400 °C.[6] This limits the fabrication temperatures that can be used for the manufacture of wearable PDs. In addition, a simple device without an external power source is favored from the perspectives of portability, size and power efficiency. To this end, research into self-powered PDs has received significant attention.[7–9] The driving force of these PDs is the internal build-in electric field, which relies on the p–n junction or the Schottky barrier to efficiently separate the photo-generated electrons and holes.[10] In order to expand the applicational domain, multifunctionality is also a highly profitable area in the field of wearable PDs.

Among PDs that allow multitasking, polarity-selective PDs have attracted rapidly growing attention. This type of photodetector (PD) features a reversible photocurrent with respect to the illuminating light wavelength. It allows the bipolar detection and transmission of optical signals within one device. For the same purpose, a conventional modulation scheme would require two PDs with filters.[11] Substantial structural simplification of the dual polarity PD evokes visions of filterless optical systems and intellectually advanced optoelectronics. To date, this peculiar, yet promising, phenomenon has been observed in optoelectronic materials including Si, p-SnS/p-Si films, HgSe quantum dots, PbS quantum dots, GaN/InGaN quantum wells and topological Dirac semimetal/MoO_3 films.[12–19] Nevertheless, their practical applications are mainly constrained by a narrow-band sensitivity, low processing rate and weak responsivity in the magnitude of μA W^{-1}. Hence, alternatives that sustain the polarity-flipping photoresponse have attracted scientific attention.

Antimony selenide (Sb_2Se_3), a p-type semiconductor, is a competitive material for use in optoelectronics and thermoelectrics. This stems from the superior carrier mobility, high absorption coefficient (in the magnitude of 10^5 cm^{-1}) and large Seebeck coefficient (661 μV K^{-1}).[20–24] On the other hand, ZnO is an n-type semiconductor that has been intensely studied owing to its wide bandgap (3.37 eV), high exciton binding energy (60 meV), environmental stability and chemical abundance.[25–27]

[a] Key Laboratory of Optoelectronic Devices and Systems of Ministry of Education and Guangdong Province, College of Physics and Optoelectronic Engineering, Shenzhen University, Shenzhen, 518060, P. R. China. E-mail: yjzeng@szu.edu.cn
[b] State Key Laboratory of Silicon Materials, School of Materials Science and Engineering, Zhejiang University, 310027, P. R. China

† Electronic supplementary information (ESI) available. See DOI: 10.1039/d1tc00786f
‡ Jinchun Jiang and Yujie Guo contributed equally to this paper.

As a representative transparent conducting oxide (TCO), ZnO has been widely used as a window layer in hetero-integrations for use in the visible-near infrared (NIR) region. Notably, the heterostructures of ZnO nanowires and Sb_2Se_3 films substantiate their potential use in polarity-selective PDs, in which Sb_2Se_3 works simultaneously as the absorber and window layer.[15] The PD arrays based on this p–n junction can be used as the current receiver in color shift keying (CSK) systems.

In this work, we develop self-powered bilayer Sb_2Se_3/ZnO photodetectors. The ZnO film serves as the window layer, hindering Sb_2Se_3 oxidation and adding a degree of freedom in the tunability of the properties. Using the diversity of hetero-combinations, the emerging polarity-reversal behavior was mechanistically explored. By taking advantage of the easily processible and programmable sputtering technique, we modulated the photoresponse through a multitude of factors. These include the device architecture, layer thickness and degree of crystallization. Upon irradiation using ultraviolet (UV)-NIR radiation, an unprecedented polarity-double-flipping phenomenon was discovered, which can be implemented by adjusting the ZnO thickness to a critical value. After performance optimization, superior properties were obtained, namely, an ultrabroad responsive band (365–1064 nm), an optimal responsivity of 77.66 mA W^{-1}, a detectivity of 2.45×10^{11} jones, and a minimal rise/decay time of 39 μs/118 μs. To the best of our knowledge, these appealing natures of flexibility and dual-polarity are embraced in a single PD for the first time. The flexible device endures 600 bending cycles with a performance degradation of only 4.38%, while retaining a localized current-flipping wavelength. This study provides further chemical and physical insights into the dual-polarity behavior. It also indicates the tantalizing opportunity of using the Sb_2Se_3/ZnO PD for speedy, sensitive, and reliable bipolar data transmission in wearable optoelectronics.

Experimental

To deposit the Sb_2Se_3/ZnO heterojunction and Au electrodes, Sb_2Se_3, ZnO and Au (4 N, 50 mm diameter with 5 mm thickness) were used, respectively. The optimal Sb_2Se_3 sputtering conditions were achieved at a power of 60 W, a working pressure of 0.5 Pa and substrate temperature of 300–350 °C. For the ZnO deposition, the optimized parameters were 60 W, 0.5 Pa and 300 °C, respectively. The heterojunction was prepared by consecutively depositing the Sb_2Se_3 and ZnO layers within a high-vacuum chamber. The *in situ* deposition was conducted either on the rigid, transparent indium tin oxide (ITO) glass, or on the flexible Au-deposited polyimide (PI) substrate. The top Au electrode was finally deposited within the area defined by the patterned mask, which was approximately 50 nm in thickness and had an approximate area of 0.005 cm^2.

X-Ray diffraction (XRD) examinations were carried out for structural and phase characterization. They were performed using a PANalytical Empyrean with a Cu Kα radiation source (λ = 0.15406 nm). The molecular vibrational modes were probed using Raman spectroscopy in a Bruker Senterra spectrophotometer with a 514 nm excitation laser. The morphologies and thicknesses of the films were extracted from the atomic force microscopy (AFM) data obtained using a AIST-NT SmartSPM, as well as from scanning electron microscopy (SEM) in Thermo APREO S, Netherlands. Compositional characterization was conducted using X-ray photoelectron spectroscopy (XPS, Thermo ESCALAB 250) with a monochromatic Al-Ka (1486.6 eV) X-ray source. A UV-visible spectrophotometer (Hitachi U-4100) was used to obtain the optical absorption spectra. To unveil the photoresponse of the PDs, current-*versus*-voltage (*I–V*) and temporal photocurrent tests were employed in the semiconductor analyzer (Keysight B2902A). The light sources for illumination were light-emitting diodes (LEDs) with monochromatic lights of 365–1064 nm. The power density was fixed at 5 mW cm^{-2} regardless of the incident wavelength. Measurement of the *in situ* power density was carried out using a power meter (Newport 1919-R) before each test. The distance between the laser and the sample was tuned to obtain the required power density on the channel.

Results and discussion

Fig. 1a displays the cross-sectional SEM image of the Sb_2Se_3/ZnO heterostructure, demonstrating the uniform thickness of the layer and well-resolved interfaces. The inset shows the homogenous surface of the heterostructure, which was verified by the AFM results shown in Fig. 1b. Upon increasing the deposition temperature from 300 to 350 °C, the Sb_2Se_3 layer yields grain boundaries. Meanwhile, the root-mean-square roughness (R_{rms}) drops slightly from 6.83 to 6.53 nm. In contrast, enhancing the ZnO coating temperature enables evident augmentation of the average grain size, which is accompanied by a substantial increase in the value of R_{rms} from 4.27 to 9.52 nm. The trend for crystallization is testified by the probes of XRD. In the Sb_2Se_3 layer deposited on the ITO substrate at 350 °C, the XRD spectrum exhibits several sharp peaks, all of which correspond to either ITO or Sb_2Se_3, as shown in Fig. 1c. This indicates the absence of impurities in the newly-grown film. The Sb_2Se_3 peaks are indexed to (020), (120), (130), (240) and (360) reflections, whereas most of them are invisible in one grown at 300 °C (JCPDS no. 15-0861). This observation reveals the transition from the amorphous to the poly-crystalline state. As shown in Fig. S1 (ESI†), the XRD pattern of the ZnO layer reveals its poly-crystallinity when deposited at 300 °C, while the ZnO XPS spectrum illustrates its pure composition and typical chemical states.[29] Next, the Sb_2Se_3 chemical stability is discussed, as it is prone to oxidation after long-term exposure to air.[28] To investigate this, we compared the composition of the pristine Sb_2Se_3 layer and the Sb_2Se_3/ZnO heterostructure several months after deposition of the layer. Fig. 1d presents the Raman spectra of these two films, containing sharp peaks at 190 and 254 cm^{-1} and a weak peak at 450 cm^{-1}. These peaks are assigned to the A_g and B_{1g} modes of Sb_2Se_3, and Sb_2O_3, respectively. The XPS results of the same Sb_2Se_3 layer confirm the chemical conversion of Sb_2Se_3. Fig. 1e presents the Sb 3d core-level XPS spectrum, which is deconvoluted into four sub-peaks. The peaks

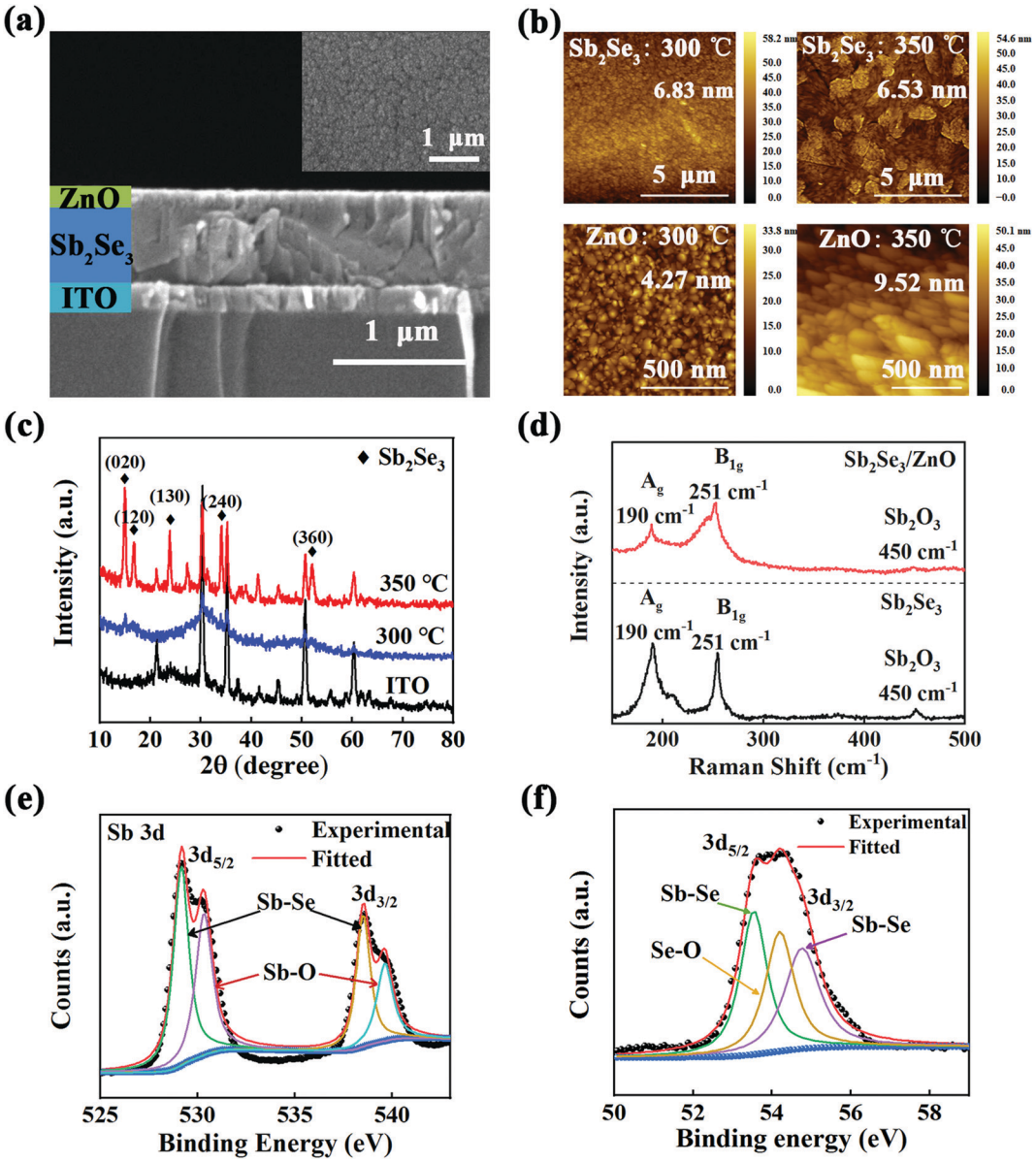

Fig. 1 Morphological and structural properties of the Sb_2Se_3/ZnO heterostructure. (a) Top-view (inset) and cross-section SEM images of the ITO/Sb_2Se_3/ZnO heterostructure. (b) AFM topological images of the thin films: Sb_2Se_3 deposited at 300 °C (top left); Sb_2Se_3 deposited at 350 °C (top right); ZnO sputtered at 300 °C (bottom left); and ZnO sputtered at 350 °C (bottom right). (c) XRD patterns of the bare ITO substrate (black curve) and the Sb_2Se_3 films sputtered at 300 and 350 °C on the ITO substrate (the blue and red curves, respectively). (d) Raman spectra of the Sb_2Se_3 film and Sb_2Se_3/ZnO heterostructure after ambient exposure for several months. (e) and (f) XPS spectra of the Sb 3d core level and Se 3d core level, respectively; the examination was performed on Sb_2Se_3 film after several months of ambient exposure.

at 529.2 and 538.6 eV correspond to Sb $3d_{5/2}$ and Sb $3d_{3/2}$ in Sb_2Se_3, whereas those at 530.3 and 539.7 eV correspond to Sb $3d_{5/2}$ and Sb $3d_{3/2}$ in Sb_2O_3. The spin–orbit splitting of 9.4 eV is well matched with results from previously published reports.[28] This observation is in good agreement with the Se 3d core-level XPS spectrum in Fig. 1f. Note that the binding energies of all identified XPS peaks were calibrated using C 1s energy at 284.6 eV. The oxidation level of Sb_2Se_3 after ambient exposure for the same duration, as revealed by the intensity of the Raman peak at 450 cm^{-1}, was suppressed after the heterogenous integration (Fig. 1d). Hence, the ZnO film serves as a protective capping to effectively prevent the Sb_2Se_3 from being oxidized. Heterostructured PDs with a vertical-electrode geometry were investigated to provide an instant collection of photon-generated carriers. A variety of channel and electrode combinations were exploited. In the Sb_2Se_3/ZnO bilayer channel, Sb_2Se_3 layers were deposited at either 300 or 350 °C, in order to interpret the role of the crystallinity in the photoresponse. On the other hand, in the 300–350 °C range, the PD performance demonstrates an inverse dependence on the ZnO coating temperature, and therefore a temperature of 300 °C was used. This trend can be explained by the progressive poly-crystallization of ZnO as discussed in the

previous section. The surface becomes rougher and the defects around the grain boundaries become denser. Both scenarios are detrimental to the construction of a suitable heterointerface that does not possess excessive surface states. Hence, the nanocrystallinity provides information about the hetero-combination. As for the electrode configuration, the initial trial was to utilize ITO and Au as the top and bottom electrodes on the rigid substrate, respectively. A diagram of the corresponding device architecture is shown in Fig. 2a, which has been named ITO/Sb_2Se_3/ZnO/Au PD. Here, discussion of the photoresponse is first focused on the visible-NIR region (405–1064 nm), so that the light absorption in ZnO under UV illumination is temporarily precluded. Fig. 2b presents the *I*–*V* curves obtained in the dark and upon visible-NIR stimuli, and the thicknesses of Sb_2Se_3 and ZnO are 330 and 60 nm, respectively. The nonlinearity and asymmetry of the curves signify the Schottky contact within the multilayer system. The corresponding time-resolved photoresponse (*I*–*t* curves) is measured under zero external bias and light illumination with a constant intensity of 5 mW cm^{-2}, as shown in Fig. 2c. The device is photo-responsive in the ultrabroad band of 365–1064 nm, and also beyond the band edge of ZnO and Sb_2Se_3. Another notable feature is the reversible polarity of the photocurrent with respect to the incident wavelengths. In the 405–685 nm incident wavelengths, the photocurrents are always negative, and become positive in the 780–1064 nm range. In comparison, the performance of the ITO/Sb_2Se_3/Au PD upon visible-NIR illumination is shown in Fig. S2 (ESI†). The photoresponse band shrinks to 365–980 nm, and the photocurrent is diminished at the incident energies close to or beyond the Sb_2Se_3 band edge. These results imply a type II band alignment at the Sb_2Se_3/ZnO heterointerface, facilitating an efficient photocarrier separation. Compared to the results shown in Fig. 2b, the *I*–*V* curves of the ITO/Sb_2Se_3/Au PD are significantly more symmetric, which reveals a shallower

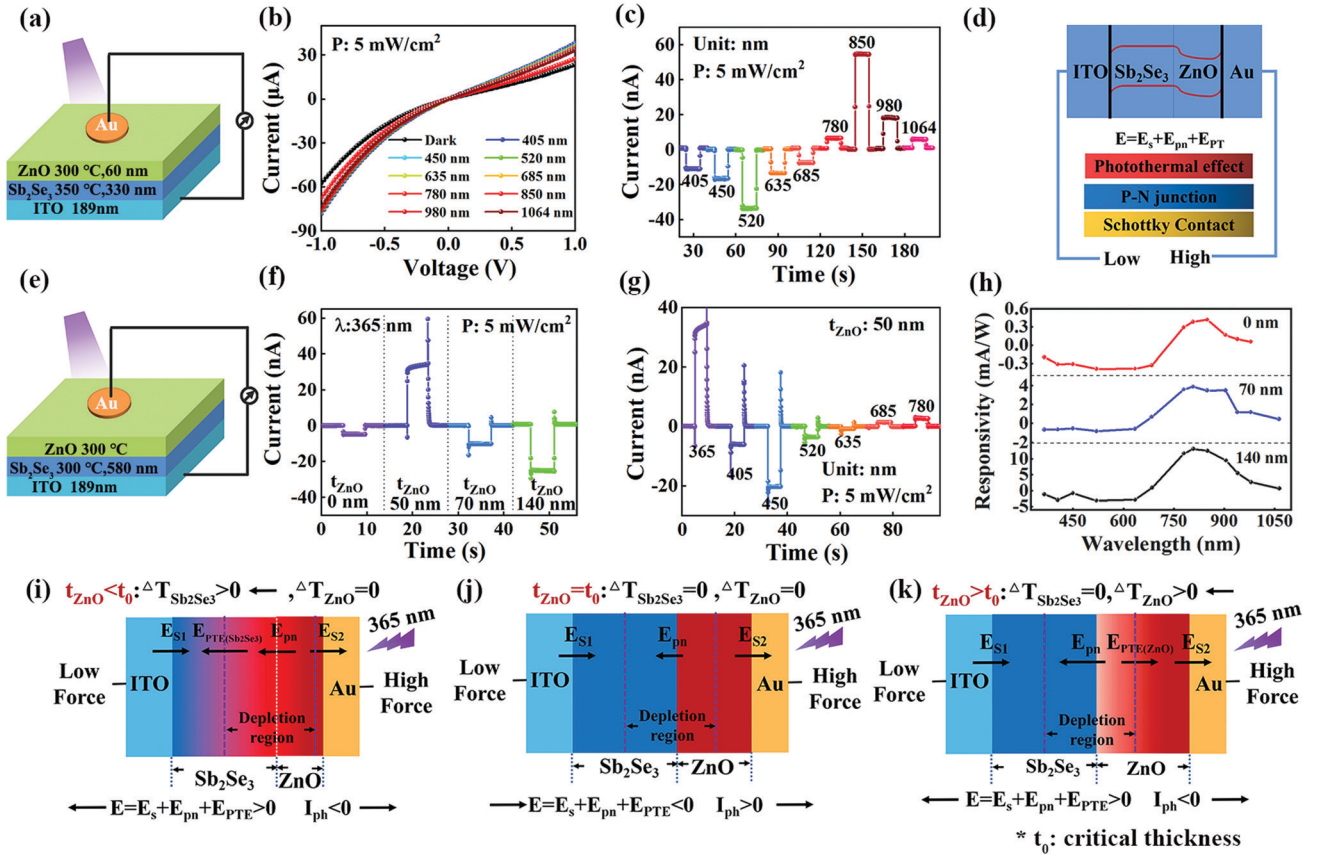

Fig. 2 Performance of the rigid PDs based on the ITO/Sb_2Se_3/ZnO/Au heterostructures. (a) A schematic diagram of the ITO/Sb_2Se_3/ZnO/Au PD, in which the ZnO layer was sputtered at 300 °C and a thickness of 60 nm, and the Sb_2Se_3 layer was sputtered at 350 °C and a thickness of 330 nm. (b) Corresponding *I*–*V* curves in the dark and under light illumination with a power density of 5 mW cm^{-2}. (c) The time-resolved photoresponse (*I*–*t* curves) under light illumination at different wavelengths (405–1064 nm) at zero bias. (d) A schematic diagram of the band alignment and working mechanism of the flexible ITO/Sb_2Se_3//ZnO/Au device PD under light illumination. (e) A schematic diagram of the ITO/Sb_2Se_3/ZnO/Au PD, in which the ZnO layer was sputtered at 300 °C and with different ZnO thicknesses (t_{ZnO}), and the Sb_2Se_3 layer was sputtered at 350 °C and with a thickness of 580 nm. (f) *I*–*t* curves of the PD with different t_{ZnO} values under 365 nm light illumination (5 mW cm^{-2}) and zero bias. (g) Self-powered *I*–*t* curves of the PD of t_{ZnO} = 50 nm under a radiation range of 365–780 nm, which demonstrates the unprecedented polarity-double-flipping behavior. (h) Comparisons of the self-powered responsivity of devices with different t_{ZnO} values upon UV-NIR exposure in the range of 365–1064 nm. (i)–(k) Mechanistic schemes for the polarity-double-flipping response in ITO/Sb_2Se_3/ZnO/Au under UV-NIR light illumination and at zero external bias. The build-in potentials with t_{ZnO} below, at, and above the critical thickness are present in (i), (j) and (k), respectively.

Schottky barrier. The switchable current polarity is also detected in the *I–t* curves of this PD, manifesting the essential role that Sb_2Se_3 plays in this peculiar phenomenon. It is also worth noting that the current flipping point is always located at 685 nm, regardless of the Sb_2Se_3 and ZnO thickness, as revealed in Fig. S2 (ESI†). In occasional cases, the point is located at 780 nm, such as in Fig. 2 for instance. We therefore infer that the current polarity is highly wavelength dependent.

In order to explicate the carrier dynamics in these PDs, we sketched the band diagrams of the ITO/Sb_2Se_3/ZnO/Au heteroassemblies. The analysis is based on the estimated work functions of ITO (4.5 eV), Sb_2Se_3 (4.82 eV), ZnO (4.65 eV) and Au (5.1 eV).[26] As shown in Fig. 2d, the Schottky barriers at the ITO/Sb_2Se_3 (E_{s1}) and ZnO/Au interfaces (E_{s2}) are both orientated from Sb_2Se_3 to ZnO, whereas the type II p–n junction creates an internal potential (E_{pn}) pointing in the reverse direction. The band alignment in the ITO/Sb_2Se_3/Au heterostructure is depicted in Fig. S2 (ESI†). Sb_2Se_3 is Schottky-contacted with the ITO electrode, and ohmic-contacted with the Au counterpart. The single side Schottky contact explains the more symmetrical *I–V* curves. Aside from these build-in potentials, the photo-thermoelectric (PTE) effect is also nonnegligible, and generates an electrical potential upon light radiation owing to the temperature gradient at the two electrodes. Driven by this field, the charge carriers at the hot end migrate towards the cold one.[30–32] Sb_2Se_3, which naturally retains a large Seebeck coefficient and absorption coefficient, is capable of constraining the photon energy within a confined dimension. Conversely, ZnO is mostly transparent in the visible-NIR wavelengths. Consequently, the PTE potential generated in this incident wavelength region is derived intrinsically from the Sb_2Se_3 layer ($E_{PTE(Sb_2Se_3)}$), pointing from the Sb_2Se_3/ZnO interface to the ITO/Sb_2Se_3 one. This orientation is opposite to that of the build-in potentials and is triggered by the p–n junction and Schottky barrier. Under these circumstance, the current direction is determined by the competition between the PTE and photovoltaic (PV) effect. Nevertheless, the existence of a temperature gradient in Sb_2Se_3 is optional. In the UV-NIR region, the absorption depth of the incident light in Sb_2Se_3 decreases monotonically as the wavelength drops.[15] Therefore, the light penetrates through the entire channel under NIR radiation. Thus, the temperature gradient across the Sb_2Se_3 layer vanishes, as does the PTE effect. The photocurrent is therefore governed only by the PV effect. This is how the current polarity flips, giving rise to the wavelength-dependent polarity-switching behavior across the visible-NIR waveband.

Analysis of the photoresponse in the ITO/Sb_2Se_3/ZnO/Au PD is then extended to the UV radiation. In this region, the photon energy exceeds the ZnO bandgap, hence, the vast majority of light is absorbed before it reaches the p–n junction interface. To study the correlation between the light absorption in ZnO and the current polarity, we engineered the ZnO thickness (t_{ZnO}) to between 0–140 nm while maintaining the Sb_2Se_3 thickness ($t_{Sb_2Se_3}$) at 580 nm (Fig. 2e). As explained in Fig. S2 (ESI†), $t_{Sb_2Se_3}$ was chosen to prohibit the incident light from penetrating through the entire channel, and to prevent a significant amount of light extinction by the bottom Au electrode. Astonishingly, the polarity of the self-powered current is highly t_{ZnO} dependent under UV light. As elaborated by the *I–t* curves in Fig. 2f, the photocurrent is negative at t_{ZnO} values of 0, 70, and 140 nm. It anomalously becomes strong and positive when t_{ZnO} = 50 nm, in contrast to its counterparts detected at 405–685 nm. Hence, the PD of t_{ZnO} = 50 nm encounters two polarity-flipping events, as shown in Fig. 2g. The current double-reversal in the UV-visible-NIR spectral breadth enriches the tunability of the PD for bipolar optical communications. More intriguingly, the double-flipping points are coincidently located at the transitional wavelengths between the two light regions; particularly at the UV-visible transitional wavelength of 365 nm, and at the visible-NIR wavelength of 685–780 nm. This endows the PD with a compelling potential for instant discrimination of the light region.

The underlying physical fundamentals of this double-flipping reaction were then explored. The discussion relies on the aforementioned PD mechanism with a trade-off between the PTE and PV effects. Based on the band alignment deduced from the ITO/Sb_2Se_3/ZnO/Au heterostructure, Fig. 2i–k schematically illustrate the build-in potentials inside the self-powered PDs that have different t_{ZnO} values under UV irradiation. Here, we define the critical thickness t_0 as the specific t_{ZnO} at which the UV light arrives right at the Sb_2Se_3/ZnO interface. If t_{ZnO} is less than t_0 (Fig. 2i), the ZnO layer cannot fully absorb all the incident photons. The residual ones create a temperature gradient inside the Sb_2Se_3 layer ($\Delta t_{Sb_2Se_3}$). The resulting $E_{PTE(Sb_2Se_3)}$ follows the direction of E_{pn}, but converse to that of E_{s1} and E_{s2}. Ultimately, the overall internal potential (E) points from the Au end towards the ITO one, resulting in a negative photocurrent. This correlates to the condition of t_{ZnO} = 0 nm. If t_{ZnO} reaches the critical value ($t_{ZnO} = t_0$), as shown in Fig. 2j, the ZnO and Sb_2Se_3 layers separately retain a homogeneous hot and cold temperature zone, resulting in the absence of E_{PTE}. Therefore, E is congruously determined by E_{s1}, E_{s2} and E_{pn}, analogous to the conditions under NIR exposure. This explains the positive photocurrent if t_{ZnO} = 50 nm. As the photocarriers are excited from both the ZnO and Sb_2Se_3 layers at 365 nm, the corresponding photocurrent yields a much higher absolute value than the visible-NIR counterparts, as revealed in Fig. 2g. Fig. 2k signifies the build-in potential under $t_{ZnO} > t_0$ and 365 nm stimuli. A temperature gradient is generated in the ZnO layer (Δt_{ZnO}), leaving the Sb_2Se_3 completely cold. This induces a PTE potential within the ZnO coating ($E_{PTE(ZnO)}$) owing to the Seebeck coefficient of -114 μV K^{-1} in the sputtered film.[33] Owing to the n-type characteristic of ZnO, the direction of $E_{PTE(ZnO)}$ is in a reverse orientation to $E_{PTE(Sb_2Se_3)}$, specifically from the inner ZnO to the Sb_2Se_3/ZnO interface. $E_{PTE(ZnO)}$ continuously drives the electrons in ZnO to migrate towards the interface, at which the depletion region blocks their way. Hence, E_{pn} becomes substantially amplified, which overwhelms the value of the sum in the opposite direction, that is, $E_{s1} + E_{s2} + E_{PTE(ZnO)}$. Consequently, the photocurrent flows in the negative direction, as indicated by the conditions of t_{ZnO}, which are 70 and 140 nm in Fig. 2f.

In order to support the above protocol for the double-flipping process under UV-visible-NIR exposure, the ZnO critical thickness t_0 is estimated. Here, we stipulate t_0 as the depth from

the ZnO surface at which 90% of incident photons have been absorbed in the pathway. At this depth, the PTE effect is hidden by the negligible heat dissipation from the weak illumination. The light intensity I_t at the penetration depth t can be expressed as:[32]

$$I_t = I_0(1 - \exp(-\alpha t)) \quad (1)$$

In which, I_0 is the light intensity on the ZnO surface radiating from the 365 nm laser (5 mW cm^{-2}), and α is the absorption coefficient of the ZnO film, as described by the following equation:

$$\alpha \frac{1}{d} \cdot \ln\left[\left(1 - R^2\right)/T\right] \quad (2)$$

in which d, R, T refer to the thickness, reflection, and transmission of the ZnO film, respectively. Therefore, α could be extracted from the simplified expression of $\alpha = 2.303A/d$, in which A is the measured absorptance at 365 nm. A is derived from the ZnO absorption spectrum shown in Fig. S2 (ESI†). We than substituted the condition $I_t = 10\%I_0$ into eqn (1), thus, acquiring the estimated t_0 = 54.34 nm. As this value is in perfect agreement with our experimental observations, it substantiates our physical findings for the t_{ZnO}-dependent current polarity at 365 nm exposure. Nevertheless, this scenario can be eliminated, merely by changing the Sb_2Se_3 sputtering temperature from 300 to 350 °C, without any variation in the ZnO thickness and incident wavelength. As discussed in Fig. 1c, this modification is significantly associated with Sb_2Se_3 crystallization. This micro process smooths the Sb_2Se_3/ZnO interface, as well as impedes the survival of defects and trap states around the interface. These interface conversions exert an evident influence on the light absorption, interface quality and eventually the photoresponse. Hence, we believe that the critical thickness t_0 could be adjusted within the nm-scale instead of being a precise value.

Together with the t_{ZnO}-dependent UV response, we also investigated the visible-NIR photoresponse modulated by t_{ZnO} and $t_{Sb_2Se_3}$. The PD performance shows a positive reliance on the thickness of the light absorber, $t_{Sb_2Se_3}$, as detailed in a previously published report.[15] The photocurrent acquired from the visible-NIR stimuli elevates monotonically with t_{ZnO} from 0 to 140 nm, with the original I–t curves of these devices displayed in Fig. S2 (ESI†). The curves showcase a minimal shifting of the polarity-flipping wavelength, proving the optical transparency of ZnO in the visible-NIR band. For better quantification, the responsivity (R) of the PDs can be calculated by using eqn (3):[34]

$$R = I_{ph}/(P \times S) \quad (3)$$

In which $I_{ph} = I_{light} - I_{dark}$; I_{ph} refers to the photocurrent, I_{light} and I_{dark} denote the current detected under illumination and in the dark, P is the intensity of the incident light (5 mW cm^{-2}) and S is the effective area of the PD (S = 0.005 cm^2), respectively. The derived R values are shown in Fig. 2h, explicitly demonstrating the photoresponse dependence on t_{ZnO}. It is well-known that the interface states, such as the traps and defects are obstacles for carrier separation and migration at the p–n junction. These states can be effectively suppressed with the progressive growth of the coating. It is therefore conceivable that the Sb_2Se_3/ZnO heterointerface is perfected by the increase of t_{ZnO} within 0–140 nm, which is instrumental to photon detection. Despite the novel and robust dual-polarity behavior, the rather limited performance hinders the practical implications of the ITO/Sb_2Se_3/ZnO/Au PD. Therefore, a more rational design for the heterogenous combination is favored, in order to avoid the back-to-back Schottky barrier while preserving the dual-polarity.

To this end, we adjusted the device architecture to that of a double-Au-electrode configuration. The Au/Sb_2Se_3/ZnO/Au assembly was sputtered onto the PI substrate, so that the viability for wearable applications could be simultaneously gauged. According to the theoretical work functions, Au/Sb_2Se_3 supports an ohmic contact. The corresponding PDs for different component parameters present their time-resolved self-powered photoresponse in Fig. 3a. The I–t curves were measured under the radiance of different wavelengths with a constant power density (5 mW cm^{-2}). Analogous to PDs prepared on the ITO substrate, the flexible PDs stick to the wavelength-dependent polarity-reversible behavior in the UV-NIR spectrum. The switching point remains at the transitional visible-NIR wavelengths of 780 nm, with a slight red-shift tendency compared to the ITO/Sb_2Se_3/ZnO/Au ones. This observation verifies the reduction of the Schottky barrier with the Au–Au electrode combination. Hence, the PTE potential required for current reversal, which is orientated in the reverse direction, becomes smaller. This explains the red-shifting trend of the polarity-flipping wavelength in the PDs with a modified configuration. In addition, compared to the ITO/Sb_2Se_3/ZnO/Au PDs, the Au/Sb_2Se_3/ZnO/Au ones demonstrate an overall photocurrent elevation, which is ascribed to the elimination of the back-to-back Schottky contact. In order to achieve functional amelioration, we tuned the ZnO thickness and Sb_2Se_3 sputtering temperature while maintaining the $t_{Sb_2Se_3}$ and ZnO deposition and temperature constant at 580 nm and 300 °C. The I–t curves of the three representative devices are shown in Fig. 3a, in order to analyze the varying tendencies. Considering the reliance of t_{ZnO} in 0–140 nm, a positive correlation is obtained, consistent with the aforementioned observation in the ITO/Sb_2Se_3/ZnO/Au PDs. The trend is embodied by the top and middle curves shown in Fig. 3a, comparing the wavelength-dependent photocurrents at t_{ZnO} of 60 and 140 nm, respectively. A maximum two-magnitude augmentation of the photocurrent was achieved in the PD of t_{ZnO} = 140 nm, which validates our previous expectation that the thicker t_{ZnO} supports a better p–n heterointerface and hence improved photon detection capabilities. Upon modulating the Sb_2Se_3 layer from the amorphous to the nanocrystalline status, the PD performance was further enhanced, as shown by comparing the middle and bottom graphs in Fig. 3a. This is implemented by sputtering the Sb_2Se_3 layers from 300 to 350 °C. The physical considerations of Sb_2Se_3 crystallization are closely related to the heterointerface dynamics. To elaborate, nanocrystallization brings about the structural periodicity, surface smoothening and defect suppression at the Sb_2Se_3/ZnO interface. The microscopic transitions facilitate the carrier separation and light absorption at the interface, which separately boosts the build-in potentials of E_{pn} and $E_{PTE(Sb_2Se_3)}$. This explains the increase in the photocurrent across the UV-NIR spectral range.

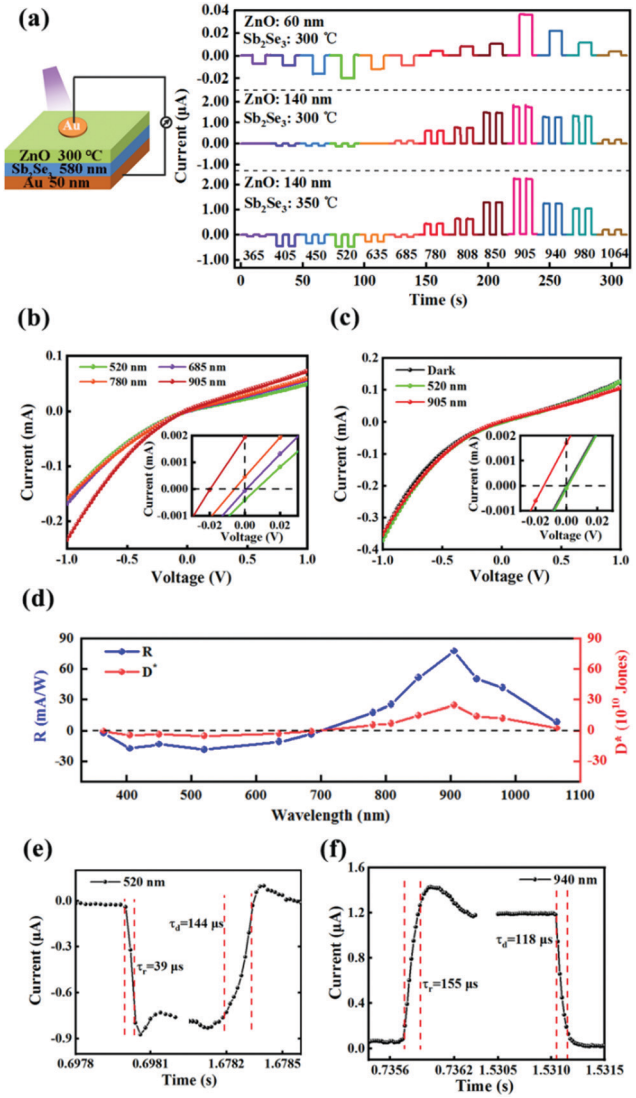

Fig. 3 Photoresponse and figures-of-merit of the flexible Au/Sb_2Se_3/ZnO/Au PDs. (a) Time-resolved photoresponses of flexible Au/Sb_2Se_3/ZnO/Au PDs prepared with different deposition parameters; the tests were conducted at zero bias and under radiance of different wavelengths in a 365–1064 nm spectral range (5 mW cm^{-2}). (b) *I–V* curves of Au/Sb_2Se_3/ZnO/Au PDs measured at zero bias under 520, 635, 685, 780, and 905 nm illumination and in the dark. The inset shows an enlarged view of the *I–V* curves around the origin. The PD was stacked by a 350 °C sputtered Sb_2Se_3 layer of 580 nm and a 300 °C sputtered ZnO layer of 140 nm. (c) *I–V* curves of the Au/Sb_2Se_3/ZnO/Au PD measured at zero bias under 520 and 905 nm illumination and in the dark. The inset shows an enlarged view of the *I–V* curves around the origin. The PD was stacked by a 300 °C sputtered Sb_2Se_3 layer of 580 nm and a 300 °C sputtered ZnO layer of 140 nm. (d) A graph of optimal *R* (blue line) and *D** (red line) values *versus* the incident wavelength (365–1064 nm). (e) The minimal rise time (τ_r) and decay time (τ_d) of the photoresponse at negative polarity, which were measured from the same PD as the one described in (c) and under 520 nm illumination. (f) The minimal rise time (τ_r) and decay time (τ_d) of the photoresponse at positive polarity, which were measured from the same PD as the one described in (c) and under 940 nm illumination.

It is notable that the enhancement in the photocurrent is more pronounced in the negative polarity range (365–635 nm). It can therefore be inferred that the Sb_2Se_3 crystallization exerts a greater influence on $E_{PTE(Sb_2Se_3)}$ than on E_{pn}. To verify this, Fig. 3b and c shows the *I–V* curves of the corresponding PDs with Sb_2Se_3 sputtered at 350 and 300 °C respectively. The highly asymmetric nature and non-linear curve confirm the influence of the PV effect. The real-time resistivity of the heterostructure is evidently increased in the 350 °C-Sb_2Se_3-sputtered PD. This observation proves the above described results that reveal that the E_{pn} becomes wider upon Sb_2Se_3 crystallization. When zooming in on the small scale around the origin, as shown in the insets, the current polarity at zero bias is in good agreement with the results shown in Fig. 3a. Furthermore, the PD containing the crystalline Sb_2Se_3 layer yields consistently higher absolute values for the current, regardless of the polarity and incident light employed. Examples illuminated under 520 and 905 nm are displayed in the insets of Fig. 3b and c.

To quantitatively interpret the optimal performance of the Au/Sb_2Se_3/ZnO/Au PDs, we extracted other key figures-of-merits. The detectivity (*D**) reflects the ability of the device to detect weak optical signals. *D** is calculated using the following equation:[34]

$$D^* = R_\lambda S^{1/2}/(2eI_{dark})^{1/2} \quad (4)$$

In which *e* is the electronic elemental charge. Fig. 3d shows the extracted R_λ and *D** with respect to the incident wavelength in the optimal Au/Sb_2Se_3/ZnO/Au PD. It can be observed that R = 77.66 mA W^{-1} and D^* = 2.45 × 10^{11} jones at 905 nm illumination, whereas R = −11.03 mA W^{-1} and D^* = 5.43 × 10^{10} jones at 520 nm radiance. Next, we concentrated on the response time of the device. Here, τ_{rise} (τ_{decay}) is defined as the interval time of the current rise (decay) from 10% (90%) to 90% (10%) of the maximum photocurrent. In the optimal flexible PD with t_{ZnO} of 140 nm and $t_{Sb_2Se_3}$ of 580 nm, the swiftest response speed is obtained when the Sb_2Se_3 layer is deposited at 300 °C. To illustrate this, Fig. 3e and f show the τ_{rise} and τ_{decay} of the device under 520 and 905 nm radiance, respectively. The minimal τ_{rise} of 39 μs and τ_{decay} of 118 μs represent an obvious improvement in the performance of reported Sb_2Se_3-based PDs.[35–38] Table 1 compares the characteristic parameters of our device with previously reported Sb_2Se_3-based PDs, as well as with those possessing polarity-flipping behaviors. It is clearly demonstrated that our flexible Sb_2Se_3/ZnO PDs exhibit a comprehensively superior performance, underpinning their potential use for optical signal processing in a speedy, sensitive, and reliable manner.

To shed light on the mechanism of action of the Au/Sb_2Se_3/ZnO/Au PD, the band alignment of the hetero-assembly was explicitly extracted. At the Sb_2Se_3/ZnO heterointerface, the valence band (VB) spectra for Sb_2Se_3 and ZnO are plotted in Fig. 4a and b. Using the linear extrapolation of the leading edge to the extended base line, the valence band maxima (VBM) values of Sb_2Se_3 and ZnO were deduced separately and found to be 0.26 and 2.36 eV below the Fermi level (E_f). Next, the conduction band minima (CBM) values were deduced from the VBM-E_g, in which E_g is the semiconductor bandgap. To estimate the E_g values of Sb_2Se_3 and ZnO, the optical absorption spectra were detected, and further deduced using the curves of $(\alpha h\nu)^n$ *versus* photo energy ($h\nu$), as shown in Fig. 4c and d.

Table 1 A comparison of the characteristic parameters for Sb_2Se_3-based photodetectors

Material	Bias/flexible	Responsivity	τ_{rise}/τ_{decay}	Ref.
Sb_2Se_3/ZnO	0 V Y^{-1}	78 mA W^{-1}@905 nm −11 mA W^{-1}@520 nm	60/179 μs@520 nm 189/118 μs@940 nm	This work
Sb_2Se_3 nanowire	10 V N^{-1} 10 V Y^{-1}	360 A W^{-1}@635 nm N/A	0.4/1.3 s@635 nm 13/20 ms@635 nm	39
Sb_2Se_3 film	5 V Y^{-1}	155 mA W^{-1}@940 nm	35/38 ms@940 nm	24
Sb_2Se_3 nanoflake	2 V N^{-1}	4320 mA W^{-1}@532 nm	13.16/9.61 ms@532 nm	21
Sb_2Se_3/ZnO	0 V N^{-1}	30.6 μA W^{-1}@880 nm −3.7 μA W^{-1}@450 nm	33/28 ms@880 nm 29/31 ms@450 nm	15
Sb_2Se_3/TiO_2	0 V N^{-1}	0.13 mA W^{-1}	14/10 ms	40
Sb_2Se_3 nanowire	5 V N^{-1}	5 A W^{-1}@405 nm	32/5 ms@405 nm	41
Sb_2Se_3/Si	0 V N^{-1}	340 mA W^{-1}@671 nm	86/96 μs@671 nm	42
SnS/ZnO	0 V N^{-1}	364 μA W^{-1}@690 nm −155 μA W^{-1}@365 nm	0.4/0.2 s	17
SnS/c-Si	0 V N^{-1}	N/A	20 μs	18

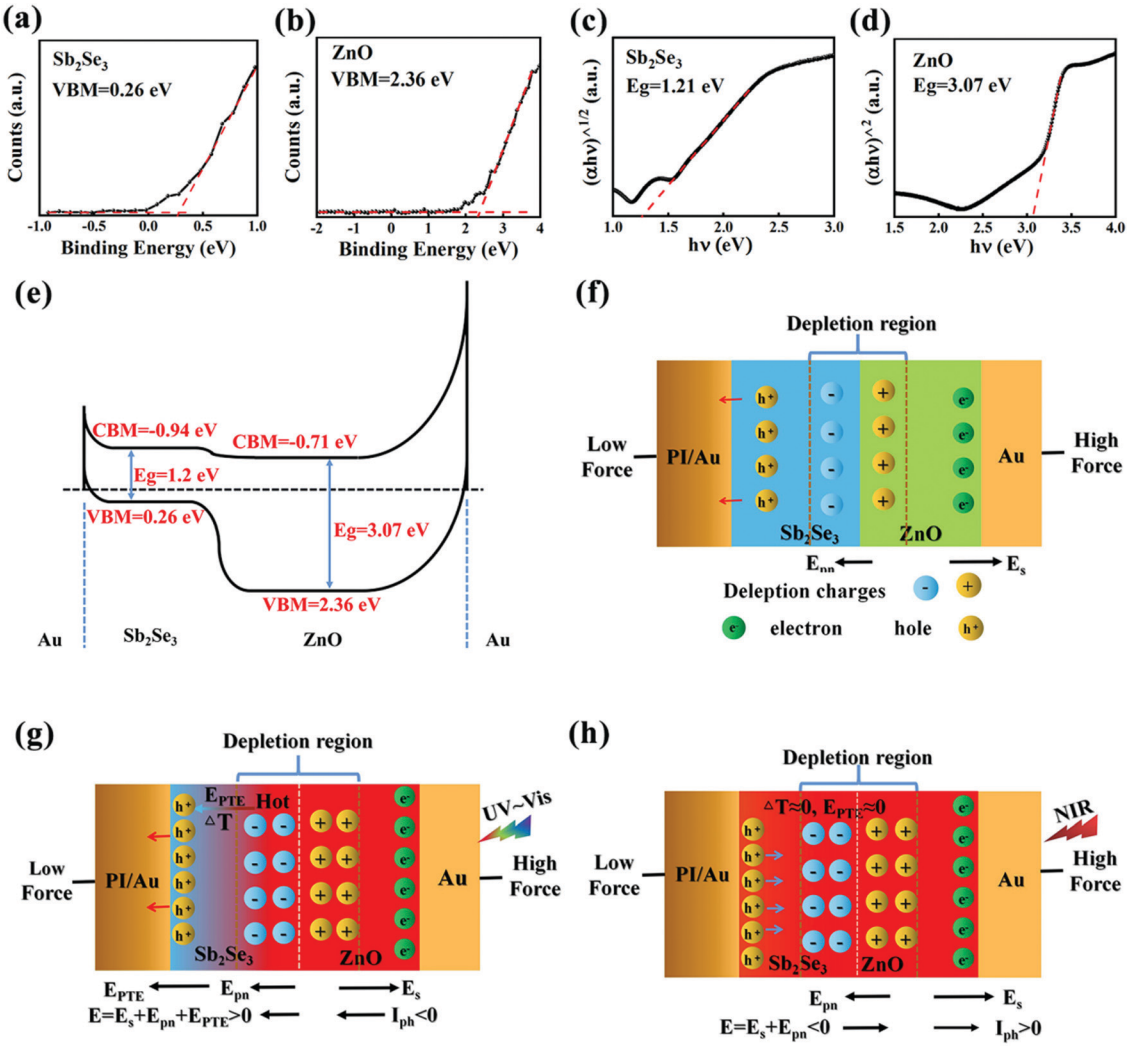

Fig. 4 The band alignment and working mechanism of the Au/Sb_2Se_3/ZnO/Au PD. The valence band edges of (a) Sb_2Se_3 and (b) ZnO. Tauc plots of (c) $(\alpha h\nu)^{1/2}$ *versus* $h\nu$ for Sb_2Se_3 and (d) $(\alpha h\nu)^2$ *versus* $h\nu$ for ZnO. (e) A band diagram of the flexible Au/Sb_2Se_3/ZnO/Au heterojunction. A schematic illustration of the PD working mechanism: (f) in the dark; (g) under UV-Vis light illumination; and (h) under NIR light illumination.

Using Tauc's equation, the E_g values of Sb_2Se_3 and ZnO were found to be to be 1.21 and 3.07 eV, respectively.[28] Hence, the corresponding CBM values are 0.95 and 0.71 eV beyond the Fermi level (E_f), respectively. Using the resembling method, the band alignment at the Au/Sb_2Se_3 and ZnO/Au interfaces were derived, as shown in Fig. S4 (ESI†). As a result, the overall band

alignment in the absence of light exposure and external biasing is plotted in Fig. 4e. A typical type II heterostructure was validated at the Sb_2Se_3/ZnO interface, whereas the Schottky barrier formed at the ZnO/Au interface favors the PV effect. The correlated internal potentials E_{pn} and E_S are schematically illustrated in Fig. 4f.

To further elaborate the carrier dynamics under light stimuli, the build-in potentials in the self-powered PD upon UV-visible and NIR radiance are demonstrated in Fig. 4g and h, respectively. Under exposure to visible-NIR light, the incident photons excite electron–hole pairs in the Sb_2Se_3 layers, while upon UV radiation the ZnO layer also participates in the photon-carrier conversion. Notably, the type-II band structure enables photon absorption to occur beyond the limitations of the bandgap. The photo-generated carriers increase the width of the depletion layer, while amplifying the Schottky barrier. Under the UV-visible light stimuli (Fig. 4g), the incident light penetrates to a limited depth in the Sb_2Se_3 layer, resulting in a substantial temperature gradient in the direction perpendicular to the layer surface. This gradient drives holes into the Sb_2Se_3 drifting from the hot end towards the cold one. Hence, the $E_{PTE(Sb_2Se_3)}$ points in the same direction as E_{pn}, but opposite to that of E_{s2}. Under these circumstances, the overall internal potential E gives rise to the negative self-powered photocurrent. On the flip side, the PTE effect is mostly absent upon NIR radiation, as the incident photons travel across the entire Sb_2Se_3/ZnO heterostructure, as shown in Fig. 4h. Hence, the NIR illumination enables a positive photo-current. This is the intrinsic process that enables the polarity-switchable photocurrent in the Au/Sb_2Se_3/ZnO/Au PD.

The feasibility of using PDs in wearable optoelectronics was determined. To investigate this, an optimal amount of Au/Sb_2Se_3/ZnO/Au PD was deposited on the PI substrate and subjected to external strain *via* repetitive bending at a radius of 8 mm. The bending set-up is illustrated in the inset of Fig. 5a. After bearing 600 bending cycles, the PD retains a broad responsive band of 365–1064 nm, as well as wavelength-selective polarity-flipping behavior. As revealed by the *I*–*t* curves shown in Fig. 5a, the flipping point is well-localized in the visible-NIR transitional wavelength region, with a minor shift from 780 to 685 nm. Hence, the flexible PD can reliably convey bi-polar optical communications even after bending. We then examined the mechanical durability of the device. This was achieved by comparing the PD performance with and without tensile strain. The results were detected under 905 nm radiance and are shown by the *I*–*V* curves in Fig. 5b and the *I*–*t* curves in Fig. 5c. Under both circumstances, the substantial increase in the curve slopes

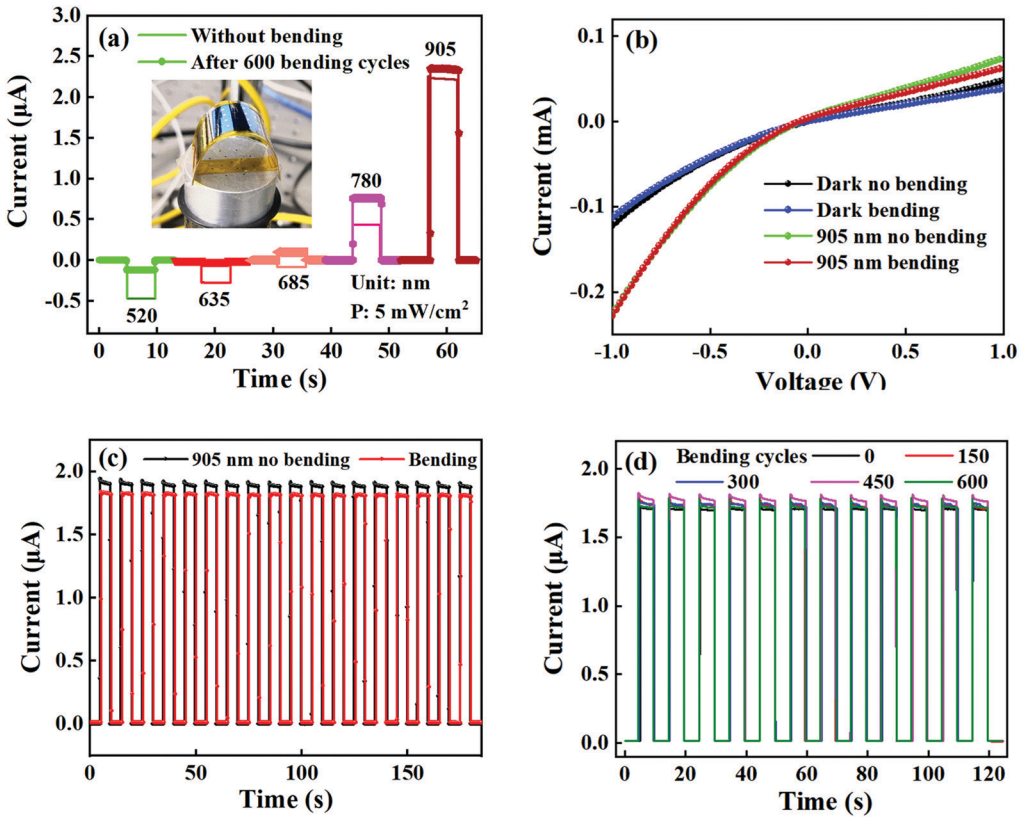

Fig. 5 Performance of the flexible Au/Sb_2Se_3/ZnO/Au PD after 600 bending cycles. (a) The time-resolved photoresponse of the PD under 520–905 nm illumination without bending and after 600 bending cycles. The inset shows a photo of the bending-test set-up. (b) *I*–*V* curves of the zero-biased PD measured under 905 nm illumination and in the dark, which compares the device performance in the presence and absence of external strain. (c) Time-resolved photoresponse of the PD with and without bending, measured under 905 nm illumination and periodic light on/off repetition cycles. (d) Time-resolved photoresponses of the PD after 0, 150, 300, 450, and 600 bending cycles, which were measured under 905 nm illumination and periodic light on/off repetition cycles.

manifests the active excitation of the photocarriers. Under both dark and illuminated situations, the *I–V* curves show minor divergence of their slopes. This observation is also explicitly elucidated by the transient photoresponse shown in Fig. 5c. The device yields a good reproducibility of the photocurrent after periodic on/off repetition, which indicates its stability under the tensile strain. Quantitatively, its responsivity only drops from $R = 77.6$ mA W^{-1} to $R = 73.53$ mA W^{-1} under bending. To better evaluate the performance degradation, Fig. 5d displays the *I–t* curves after 150, 300, 450, and 600 bending cycles. Negligible device deterioration is observed, even with a slightly enhanced photocurrent. A similar trend is observed under illumination at 520 nm, as shown in Fig. S5 (ESI†). It is worth mentioning that the current variation exhibits a peculiar tendency during and after bending. When subject to strain, the current experiences a decline regardless of the radiant wavelength. Nevertheless, when removing the external stress, the absolute values of the current in the negative direction are always lower than, or close to, the original ones, whereas the counterparts in the positive direction are slightly elevated. This trend, together with the small blue-shift of the polarity-flipping point, indicates that the decrease in E_{pn} is effected by the residual strain. The scenario can be explained by the ZnO piezo-electric effect, which results in band-bending that facilitates carrier separation.[6] This polarity-dependent trend in current fluctuation vanishes in a device that has undergone bending, owing to the additional yet adverse impacts from the structural deformation. Within the spectral range of 405–1064 nm, a performance degradation of only 4.38% was detected. To further study the impact of the tensile strain, channel folding with smaller bending radii of 4 and 6 mm was also employed. Thus, the strain was increased up to 0.45% at the bending radius of 4 mm. Fig. S5c (ESI†) displays the *I–t* curves of the PD under 905 nm illumination and external strain of various bending radii. Under all circumstances, the *I–t* curves retain a good reproducibility against repetitive folding. With a reduced bending radius, the influence of the piezo-electric effect surpasses the bending-induced film degradation. As a result, the photocurrent undergoes an additional increase after bending. It is worth noting that a bending radius of 6 mm gives rise to the maximal photocurrent, whereas the 4 mm counterpart shows a sacrifice in both the responsivity and stability, as shown in Fig. S5c (ESI†). From this perspective, the bending radius of 6 mm (0.3% tensile strain) represents the optimal condition. The substantial photocurrent enhancement and strong flexible durability indicates the self-powered Au/Sb_2Se_3/ZnO/Au device is a promising candidate for use in wearable applications.

Conclusions

In this work, we demonstrated the fabrication of flexible self-powered PDs based on a bilayer Sb_2Se_3/ZnO heterostructure. The devices present dual current polarities with respect to the incident wavelength. This phenomenon is ascribed to a trade-off between the PTE effect and the PV effect triggered by the Schottky barrier and p–n junction. Across the critical thickness of the ZnO layer, an unprecedented double-polarity-flipping photoresponse was observed upon UV-NIR radiation. In the visible-NIR region, the polarity-flipping behavior is tailorable *via* multiple routes. Aside from the light absorber of Sb_2Se_3, the influences of the window layer and the electrode are discussed for the first time. All relevant parameters, including the layer component, thickness, and deposition temperature, intrinsically impact the heterogeneous band alignment, the destination of the penetrating light, and the interfacial quality. The optimal PD demonstrates a comprehensive advance in performance, including an ultrabroad responsive band (365–1064 nm), an optimal responsivity of 77.66 mA W^{-1}, a detectivity of 2.45×10^{11} jones, and minimal rise/decay times of 39 μs/118 μs. The exciting features of dual-polarity are creatively combined into flexible devices. The PDs possess excellent stability and durability after 600 bending cycles, with a well-localized polarity-switching wavelength. This study underpins the feasibility and reliability of this device for dynamic, wearable, and bipolar optical data transmission. It provides tantalizing opportunities for a plethora of applications, for example, the instant discrimination of incident wavelength regions, advanced intelligence optoelectronics, and so on. Our study also paves the way for the delicate design and optimization of polarity-flipping PDs based on arbitrary hetero-assemblies.

Conflicts of interest

There are no conflicts to declare.

Acknowledgements

This work was supported by the Shenzhen Science and Technology Project under Grant No. JCYJ20180507182246321. We thank the Instrument Analysis Center of Shenzhen University for assistance with the SEM analysis.

References

1 C. Xie and F. Yan, *Small*, 2017, **13**, 1701822.
2 J. Yao and G. Yang, *Small*, 2018, **14**, 1704524.
3 T. Dong, J. Simões and Z. Yang, *Adv. Mater. Interfaces*, 2020, **7**, 1901657.
4 S. Cai, X. Xu, W. Yang, J. Chen and X. Fang, *Adv. Mater.*, 2019, **31**, 1808138.
5 Y. Lei, J. Luo, X. Yang, T. Cai, R. Qi, L. Gu and Z. Zheng, *ACS Appl. Mater. Interfaces*, 2020, **12**, 24940.
6 Y. Guo, L. Zhang, D. Jin, Y. Lu, Z. Xu, J. Jiang, Z. Yang, H. Liang, H. Fang, S. Ruan and Y.-J. Zeng, *Adv. Opt. Mater.*, 2021, **9**, 2001551.
7 Z. Wen, J. Fu, L. Han, Y. Liu, M. Peng, L. Zheng, Y. Zhu, X. Sun and Y. Zi, *J. Mater. Chem. C*, 2018, **6**, 11192.
8 Y. Zhang, M. Peng, Y. Liu, T. Zhang, Q. Zhu, H. Lei, S. Liu, Y. Tao, L. Li, Z. Wen and X. Sun, *ACS Appl. Mater. Interfaces*, 2020, **12**, 19384.

9 L. Han, M. Peng, Z. Wen, Y. Liu, Y. Zhang, Q. Zhu, H. Lei, S. Liu, L. Zheng, X. Sun and H. Li, *Nano Energy*, 2019, **59**, 492.
10 W. Tian, Y. Wang, L. Chen and L. Li, *Small*, 2017, **13**, 1701848.
11 W. Xu, H. Shen, J. Wang and H. Zhang, *Electron. Lett.*, 2016, **52**, 133.
12 C. Yang, S. P. Turaga, A. A. Bettiol, P. Balamuniappan, M. Bosman, H. R. Tan, J. H. Teng and E. J. Teo, *ACS Photonics*, 2017, **4**, 443.
13 L. Shen, Y. Zhang, Y. Bai, X. Zheng, Q. Wang and J. Huang, *Nanoscale*, 2016, **8**, 12990.
14 X. Tang, G. f. Wu and K. W. C. Lai, *J. Mater. Chem. C*, 2017, **5**, 362.
15 B. Ouyang, H. Zhao, Z. L. Wang and Y. Yang, *Nano Energy*, 2020, **68**, 104312.
16 B. Yin, H. Zhang, Y. Qiu, L. Luo, Y. Zhao and L. Hu, *Nanoscale*, 2017, **9**, 17199.
17 K. Z. A. Y. Bangsen Ouyang, *iScience*, 2018, **1**, 16.
18 M. Patel, M. Kumar and J. Kim, *J. Mater. Chem. C*, 2018, **6**, 6899.
19 M. Yang, Y. Yang, Q. Liu, H. Zhou, J. Han, X. Xie, F. Xiu, J. Gou, Z. Wu, Z. Hu, T. Yu, J. Wang and Y. Jiang, *J. Mater. Chem. C*, 2020, **8**, 16024.
20 T. Zhai, M. Ye, L. Li, X. Fang, M. Liao, Y. Li, Y. Koide, Y. Bando and D. Golberg, *Adv. Mater.*, 2010, **22**, 4530.
21 M. Zhao, J. Su, Y. Zhao, P. Luo, F. Wang, W. Han, Y. Li, X. Zu, L. Qiao and T. Zhai, *Adv. Funct. Mater.*, 2020, **30**, 1909849.
22 H. Song, T. Li, J. Zhang, Y. Zhou, J. Luo, C. Chen, B. Yang, C. Ge, Y. Wu and J. Tang, *Adv. Mater.*, 2017, **29**, 1700441.
23 G. Chen, W. Wang, C. Wang, T. Ding and Q. Yang, *Adv. Sci.*, 2015, **2**, 1500109.
24 X. Wen, Z. Lu, L. Valdman, G. Wang, M. Washington and T. Lu, *ACS Appl. Mater. Interfaces*, 2020, **12**, 35222.
25 Y. J. Zeng, Z. Z. Ye, W. Z. Xu, D. Y. Li, J. G. Lu, L. P. Zhu and B. H. Zhao, *Appl. Phys. Lett.*, 2006, **88**, 062107.
26 L. Hu, J. Yuan, Y. Ren, Y. Wang, J. Q. Yang, Y. Zhou, Y. J. Zeng, S. T. Han and S. Ruan, *Adv. Mater.*, 2018, **30**, 1801232.
27 B. Deka Boruah, *Nanoscale Adv.*, 2019, **1**, 2059.
28 A. Dutta, R. Singh, S. K. Srivastava and T. Som, *Sol. Energy*, 2019, **194**, 716.
29 L. Hu, Q. Liao, Z. Xu, J. Yuan, Y. Ke, Y. Zhang, W. Zhang, G. P. Wang, S. Ruan, Y. Zeng and S. Han, *ACS Photonics*, 2019, **6**, 886.
30 X. Lu, L. Sun, P. Jiang and X. Bao, *Adv. Mater.*, 2019, **31**, 1902044.
31 Y. Guo, Y. Song, M. Yang, Z. Xu, H. Xie, H. Li, Z. Li, H. Liang, S. Ruan and Y.-J. Zeng, *J. Mater. Chem. C*, 2020, **8**, 13226.
32 M. Buscema, M. Barkelid, V. Zwiller, H. S. J. van der Zant, G. A. Steele and A. Castellanos-Gomez, *Nano Lett.*, 2013, **13**, 358.
33 T. T. P. Dai Cao Truong, H. K. T. T. Truong Huu Nguyen and V. C. Tran, *Sci. Tech. Dev. J.*, 2020, **23**, 788.
34 J. Yuan, L. Hu, Z. Xu, Y. Zhang, H. Li, X. Cao, H. Liang, S. Ruan and Y. Zeng, *J. Phys. Chem. C*, 2019, **123**, 14766.
35 M. Wang, W. Tian, F. Cao, M. Wang and L. Li, *Adv. Funct. Mater.*, 2020, **30**, 1909771.
36 W. Tian, L. Min, F. Cao and L. Li, *Adv. Mater.*, 2020, **32**, 1906974.
37 T. Huo, H. Yin, D. Zhou, L. Sun, T. Tian, H. Wei, N. Hu, Z. Yang, Y. Zhang and Y. Su, *ACS Sustainable Chem. Eng.*, 2020, **8**, 15532.
38 F. Cao, W. Tian, L. Meng, M. Wang and L. Li, *Adv. Funct. Mater.*, 2019, **29**, 1808415.
39 Y. Liang, Y. Wang, J. Wang, S. Wu, D. Jiang and J. Lian, *RSC Adv.*, 2016, **6**, 11501.
40 J. Wang, S. Li, T. Wang, F. Guan, L. Zhao, L. Li, J. Zhang and G. Qiao, *ACS Appl. Mater. Interfaces*, 2020, **12**, 38341.
41 Z. Ma, S. Chai, Q. Feng, L. Li, X. Li, L. Huang, D. Liu, J. Sun, R. Jiang, T. Zhai and H. Xu, *Small*, 2019, **15**, 1805307.
42 G. Li, Z. Li, J. Chen, X. Chen, S. Qiao, S. Wang, Y. Xu and Y. Mai, *J. Alloys Compd.*, 2018, **737**, 67.

